Electronic Response Properties of Carbon Nanotubes in Magnetic Fields

Daniel Sebastiani[†,*] and Konstantin N. Kudin[‡]

[†]Max-Planck-Institute for Polymer Research, Ackermannweg 10, 55128 Mainz, Germany, and [‡]Princeton Institute for Science and Technology of Materials (PRISM), Princeton University, Princeton, New Jersey 08544

ABSTRACT Magnetic linear response properties for achiral and chiral carbon nanotubes were investigated with first-principles electronic structure methods. We have computed the magnetic shielding inside and outside the tubes originating from electronic current densities induced by the application of an external magnetic field. This electronic response of the nanotubes was analyzed for external magnetic fields both parallel and perpendicular to the tube axis. The magnetic screening would be experienced by guest molecules inside the tubes, measurable by NMR spectroscopy on isotopically labeled samples. Special attention is given to chiral nanotubes, in which longitudinal fields induce a non-zero longitudinal current density and thus tangential magnetic fields outside the tubes.

KEYWORDS: carbon nanotubes · nuclear magnetic resonance · nucleus-independent chemical shift maps · density functional theory · guest–host complexes

Since their discovery, carbon nanotubes (CNTs) have attracted an ever increasing interest from various research directions in physics, chemistry, and biology.[1,2] A wealth of literature exists on the topic of CNTs,[3,4] including detailed studies of their optical,[5] mechanical, and electrical properties.[6–8] The transverse and longitudinal electronic response to electric fields has recently been studied theoretically,[9–12] along with experimental capacitance and conductance properties.[13] Also, the aromatic character of CNTs has been the subject of a series of investigations.[14,15] NMR chemical shifts for carbon atoms and adsorbed species have been reported very recently, obtained from both experiments[16–19] and theoretical calculations.[20–23] Upon isotope substitution, shifts in Raman resonance lines have been shown to provide valuable information about structural properties of double-wall CNT systems.[24]

However, to the best of our knowledge, no systematic investigation exists of the generalized host–guest shifts of molecules trapped inside CNTs. Such information can be gained from the nucleus-independent chemical shift (NICS)[25] calculations that yield three-dimensional NICS maps.[23] In practical terms, the NICS maps allow one to predict the magnetic screening effect of nanotubes on any molecular complexes both outside and inside the nanotubes without carrying out the actual calculation, provided that the interactions between guest–host species are weak. In the case of CNTs, this assumption is true for a variety of guest molecules. In terms of the actual computational procedure, the spatial NICS maps are generated by analyzing induced current densities and induced magnetic fields inside and outside the tubes.[23] In this work, we calculate the NICS maps for a series of nanotubes of varying diameter and chirality, with the objective to facilitate the experimental interpretation of the chemical shifts observed for host–guest systems involving CNTs.

Our computational predictions would be of interest to the ongoing research utilizing nanotubes as transport channels to carry fluids, helping to understand water behavior inside such tubes.[17,26,27] The knowledge of the host–guest interactions also allows one to probe the hydrogen positions when using nanotubes for storage applications[28,29] and to observe the trapping of xenon.[16] Finally, with the recent advances in nanotube growth on non-magnetic metal nanoparticles such as copper or gold,[30,31] NMR studies of nanotube systems with molecules trapped inside are going to become much more common.

As a side comment, host–guest complexes are an intriguing subject by themselves,[32,33] since atomistic knowledge of the underlying interactions permits the design of materials with specific functionalities, such as in the areas of drug delivery and molecular recognition as well as molecular sieves.[34–36] But also from a more funda-

*Address correspondence to sebastia@mpip-mainz.mpg.de.

Received for review August 6, 2007 and accepted March 04, 2008.

Published online March 26, 2008.
10.1021/nn700147w CCC: $40.75

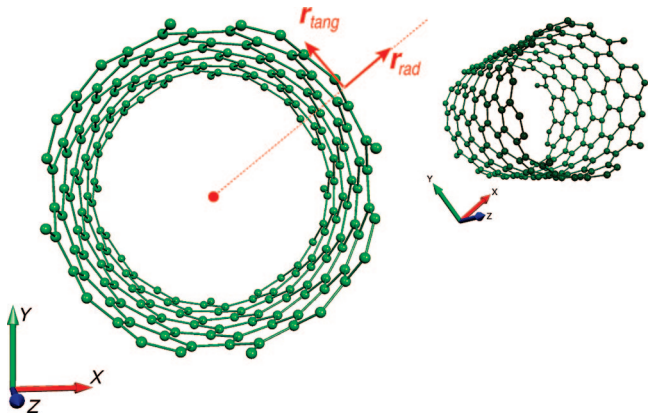

Figure 1. Illustrations of the geometry of a bare (12,4) carbon nanotube, together with the orientation of the coordinate system used throughout this work.

mental point of view, the presence and the motion of guest molecules confined in nanostructures such as CNTs is a topic of great interest.[37]

The overall structure of the paper is the following. We first discuss the standard magnetic properties of nanotubes that are commonly calculated in the literature, such as ^{13}C shifts and magnetic susceptibilities. Next, we report magnetic fields induced inside of achiral, chiral, and double-wall nanotubes. Then, we focus in detail on the unusual magnetic properties of chiral nanotubes, specifically the peculiar induced tangential and radial current densities. Finally, we conclude. The details of our computational methodology are described in the last section of the paper.

RESULTS AND DISCUSSION

Chiral and Non-chiral Carbon Nanotubes. An example of a typical nanotube is given in Figure 1, and in Table 1 we summarize the numerical results from our calculations. Compared to the earlier calculations of ^{13}C shifts,[20] we find that our shifts are ~10 ppm smaller for equivalent tubes, which is probably due to the differences in the implementation and calculation parameters. The chiral nanotubes fall into the same range. In addition, we also observe a relatively small dependence of the ^{13}C shift on the nanotube diameter, with smaller diameter tubes having larger shifts. For a detailed analysis of the nanotube shift as a function of tube diameter, we refer the reader to an earlier work.[20]

TABLE 1. ^{13}C Shifts for Carbon Atoms, Nucleus-Independent Chemical Shift Values inside CNTs (in ppm), and Diagonal Elements of the Magnetic Susceptibility Tensor (in Units of 10^{-30} J/T^2 per Carbon Atom) as a Function of the Tube Vector[a]

tube	δ_C^{TMS}	NICS	χ_{xx}^m	χ_{zz}^m	D	L
(6,2)	130	−29	−233	−133	5.69	15.39
(6,4)	127	−30	−285	−104	6.86	18.59
(8,4)	124	−34	−319	−180	8.32	22.57
(10,0)	122	−36	−319	−193	7.86	17.07
(10,5)	121	−39	−397	−199	10.38	22.57
(11,0)	120	−43	−376	−224	8.64	17.07
(12,4)	107	−57	−533	−362	11.32	15.38
(13,0)	116	−46	−427	−312	10.20	17.06
(14,0)	115	−50	−477	−319	10.99	17.06
(16,0)	111	−53	−543	−428	12.55	17.06
(17,0)	111	−57	−601	−454	13.33	17.06
(19,0)	110	−60	−675	−581	14.22	17.06
(10,0)@(19,0)	61/113	-60^b / -95^i	−537	−446		17.06

[a] For the double-wall tube (10,0)@(19,0), the superscript *b* refers to the area between the tubes, while *i* corresponds to the region inside the inner CNT. The nanotube diameter D and the supercell length L along the Z axis are given in angstroms.

The NICS values in the center of the nanotubes, given in Table 1, indicate the increase of the shielding with the nanotube diameter, which is opposite to the trend observed for the ^{13}C shifts. We note that the very large NICS values of −30 to −60 ppm are only valid under the assumption of a defect-free, perfectly periodic and thus infinite nanotube. For real tubes, these values will be lower due to defects and the finite length.

The diagonal elements of the magnetic susceptibility tensor are also shown in Table 1. Note that for our orientation of the tubes (tube axis parallel to the Z axis), $\chi_{xx} = \chi_{yy}$. Having discussed the overall picture and commonly encountered magnetic properties, we now turn our attention to the detailed behavior of specific nanotubes.

Induced Magnetic Field in Non-chiral Nanotubes. As indicated by the earlier preliminary studies,[23] the induced shielding fields inside CNTs are expected to be quite large, because the high degree of delocalization of the aromatic orbitals gives rise to strong currents both parallel to the tube and ring-like in the perpendicular plane. To illustrate the typical behavior of the NICS values inside the nanotube, representative plots of slices of

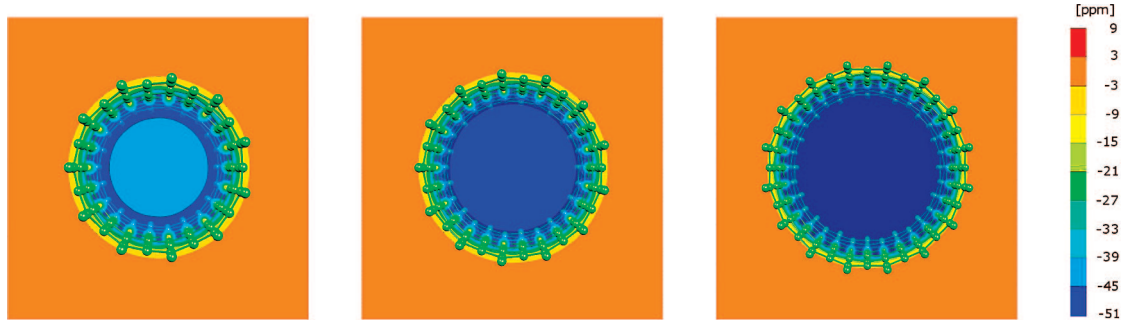

Figure 2. NICS maps for non-chiral carbon nanotubes of (11,0), (13,0), and (16,0) type.

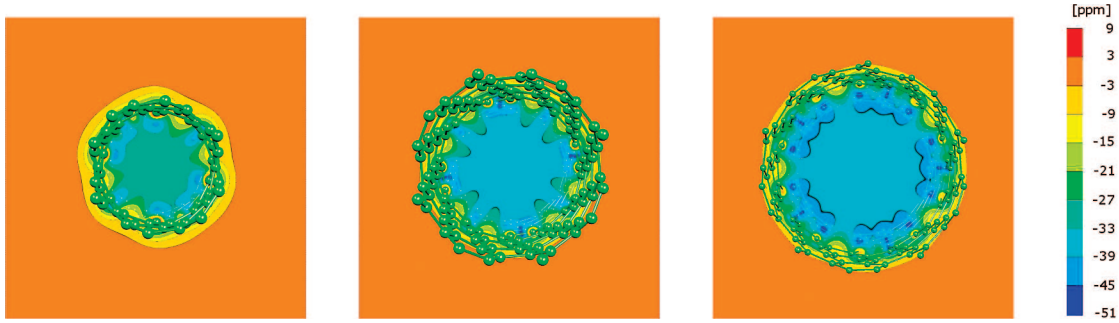

Figure 3. NICS maps for a set of chiral carbon nanotubes of (6,2), (8,4), and (10,5) type.

NICS maps for three (*n*,0) nanotubes are shown in Figure 2.

The green and cyan colors indicate relatively homogeneous NICS values of about −45 to −60 ppm, which is considerably more intense than the induced field of about −10 ppm in the region around 1 Å on top of the center of an isolated benzene ring.

Induced Magnetic Field in Chiral Nanotubes. For a chiral (*n*,*m*) nanotube with $m \neq 0$ (and $(n - m)$ not divisible by 3), the unit cell size is significantly bigger, and the lattice vector along the axial direction is significantly longer than it is for achiral tubes. While non-chiral CNTs always have a periodicity of 4.27 Å, the minimum unit cell required for a (6,4) CNT is about 18.6 Å long. The (12,4) nanotube shown in Figure 1 in turn has a periodicity of 15.4 Å.

The reduced symmetry has consequences regarding the electronic response to the external magnetic perturbation. In Figure 3, the isotropic NICS maps for a series of chiral nanotubes are plotted, using the same color coding as in Figure 2. The shieldings are quite close to those of the non-chiral tubes, although the electronic currents can no longer circulate in an optimal way (orthogonal to the applied field) but instead are forced to go along the chemical bonds of the tube.

Also, inside the tube, the induced local field is somewhat less homogeneous than in the non-chiral tubes. This is particularly visible in the (10,5) nanotube, which can be contrasted with its (10,0) counterpart (Figure 4; see also Table 1).

Coaxial Double-Wall Carbon Nanotubes. Going beyond the single-wall CNTs (SWNT), we now apply the NICS concept to coaxial double-walled tubes (DWNT). As in the case of SWNTs, the high degree of delocalization of the aromatic orbitals creates strong currents and thus considerable magnetic shielding fields. However, since there are now two independent electron clouds available to screen the external magnetic field, the lower-frequency shifts in the NICS maps inside DWNTs are expected to be even more pronounced.

The NICS maps for such a system, as well as for its individual nanotubes by themselves, are shown in Figure 4 (note that the scale is different from that of Figures 3 and 2). The left and middle parts display the NICS maps for single-wall (10,0) and (19,0) tubes, where the NICS values reach similar values as for the tubes shown in Figures 3 and 2. The induced field increases to −100 ppm when the two tubes are nested, forming a double-wall CNT. While the region between the tubes retains the NICS value of the isolated (19,0) tube, the shielding is superimposed in the inner area of the (10,0) CNT. This is not unexpected, since the interaction between the nanotubes is only of the weak van der Waals nature. Furthermore, in our approach, the induced magnetic field is computed as a linear response property and thus is additive for weakly interacting tubes. Overall, the magnetic fields created by the outer nanotube response are in the ppm (1/1000000) range and thus have an insignificant effect on the response of the inner tube. This is in stark contrast to how coaxial nanotubes behave in external *electric* fields, where the response of the electronic density of the outside nanotube is capable of almost completely shielding the external field for the inner tube.[11]

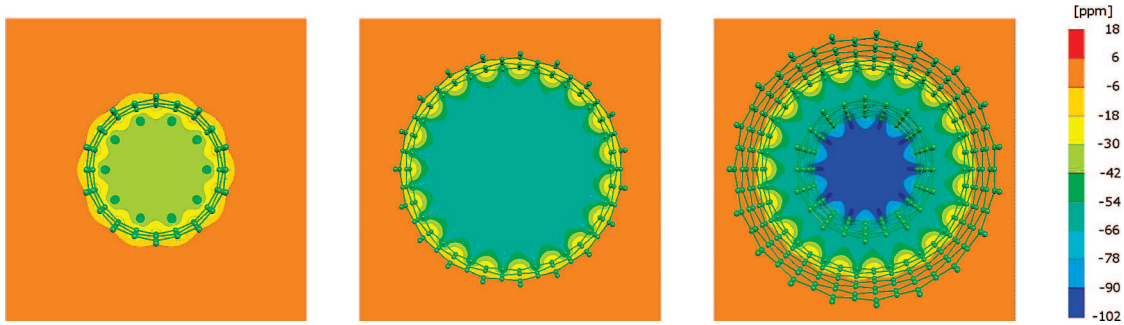

Figure 4. Left and middle: Induced magnetic field maps of a (10,0) and a (19,0) CNT. Right: The same map for a (10,0) tube located inside a (19,0) CNT (double-wall tube). Note that the color scale is the same for all three plots, but different from the one used in Figure 2.

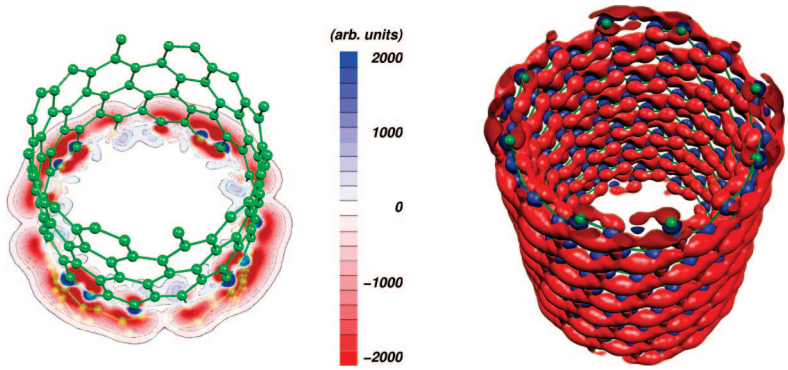

Figure 5. Left: Contour map of the tangential current density j^{ind}_{tang} of a (12,4) CNT, with clockwise and counter-clockwise currents plotted in blue and red. For the definition of the tangential current, see eq 2. Right: Isosurface of the same j^{ind}_{tang}, taken at the maximum value of the contour map (2000 arbitrary units). The external field is oriented along the *Z* axis.

In our coaxial system, the isotropic carbon nuclear shielding of the (10,0) tube inside the (19,0) CNT is shifted by 61 ppm to lower frequency, which is consistent with the predictions from the NICS field of the (19,0) tube (Table 1). Additionally, this plot indicates that there is little influence of the electronic subsystem of one tube on the other, leaving the aromatic character of both nanotubes almost unchanged. This is not surprising, since the distance between the nanotube walls is 3.7 Å, and the mobile π densities reside outside of the tubes, so they do not come into a contact with each other.

Note that in a previous *ab initio* study,[20] a significantly smaller shielding effect has been found. Specifically, for an (8,0)@(16,0) tube, the inner one was only −21 ppm shifted with respect to an isolated (8,0) CNT, compared to our NICS value of −53 ppm from Table 1 for the (16,0) type. Having only access to our NMR implementation, we cannot elucidate the origin of this discrepancy. Nevertheless, both the trend and the magnitude of the shielding effect in SWNTs that we predict appear to be in reasonable agreement with the existing experiments for water in nanotubes.[18]

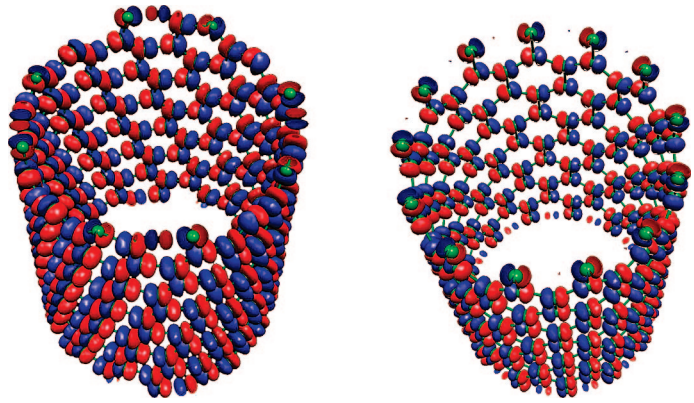

Figure 6. Isosurfaces of the radial current density j^{ind}_{rad} according to eq 1 of a (12,4) and a (13,0) nanotube, respectively, using the same surface value as in Figure 5.

Chiral Tubes—Chiral Currents. ***Current Density Decomposition.*** The orbital electronic response of CNTs to an external magnetic field results in a shielding magnetic field, the direction of which is opposite to the external one, just like it is for nanotubes in static *electric* fields.[9,10] This behavior can be understood in terms of the current densities induced by the magnetic field, which we have computed and analyzed. Because the interesting effects are observed mostly for longitudinal fields, and unless otherwise noted, in the following we will consider an external magnetic field along the tube axis, which is chosen to be aligned with the *Z* axis (see Figure 1).

Naturally, such a *Z* field induces non-zero current components along all three Cartesian axes. For clarity of the discussion, we convert them into longitudinal, radial, and tangential current components. The longitudinal current density j^{ind}_{z} is simply the *Z* element of the Cartesian current density vector. The other two Cartesian components of the currents induced in the directions orthogonal to the nanotube axis can be transformed into radial j^{ind}_{rad} and tangential j^{ind}_{tang} in-plane vectors. The radial component of the current density is defined as

$$j^{ind}_{rad}(\mathbf{r}) = \hat{\mathbf{r}}_{rad} \cdot \mathbf{j}^{ind}(\mathbf{r}) \quad (1)$$

where $\hat{\mathbf{r}}_{rad}$ is the normalized coordinate vector in the (*x*,*y*)-plane with respect to the centered nanotube axis (see also Figure 1). The tangential in-plane current j^{ind}_{tang} is computed as

$$j^{ind}_{tang}(\mathbf{r}) = \hat{\mathbf{r}}_{tang} \cdot \mathbf{j}^{ind}(\mathbf{r}) \quad (2)$$

where $\hat{\mathbf{r}}_{tang}$ is the vector tangential to the tube (also illustrated in Figure 1).

Tangential and Radial Current Densities. The tangential current is shown in Figure 5 for a (12,4) CNT, both as a contour map and as isosurface. The different orientations (clockwise and counter-clockwise) of the current are plotted in blue and red, respectively. These plots illustrate the dominance of the "shielding" orientation over the "deshielding" component. The radial currents are shown in Figure 6 for (12,4) and (13,0) nanotubes. Again, the different orientations (away from and toward the tube center) of the current are plotted in blue and red, respectively. They illustrate that there are localized atom-centered currents around each carbon atom, and they are similar for chiral and non-chiral tubes.

Note, however that such localized current densities do not contribute to the strong shielding inside the CNTs.

On one hand, these plots show that there are considerable localized and atom-centered currents in-

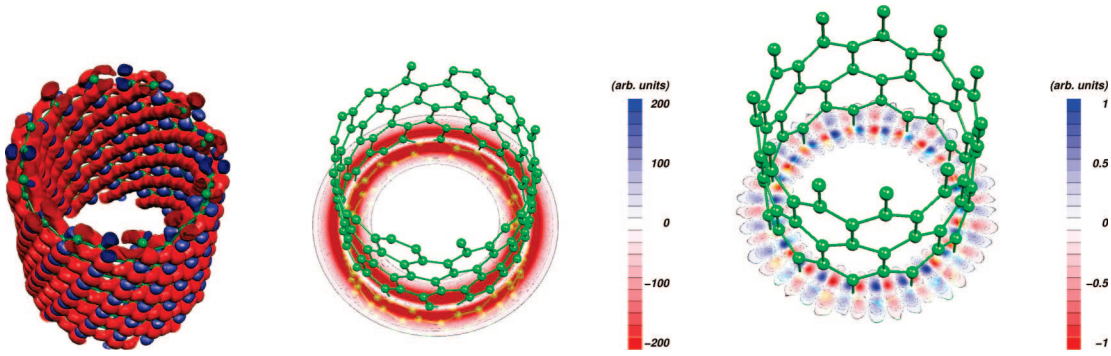

Figure 7. Left: Isosurface of the *longitudinal* component of the current density j_z^{ind} for a (12,4) CNT with the external field along *Z*. Middle/right: Component of this longitudinal current density within the (*x*, *y*)-plane ($j_{proj,z}^{ind}$ according to eq 3) for a chiral (12,4) and a non-chiral (11,0) nanotube. Note also the different color codings: the scale for the non-chiral CNT is zoomed by a factor of 200 with respect to the (12,4) tube.

duced by the external magnetic field just like in any other system with atomically localized electronic orbitals. On the other hand, there are somewhat weaker yet significantly more-delocalized current densities flowing around the tube along much longer paths defined by the C−C bonds. This delocalized current is essentially absent on the inner side of the CNT, as illustrated by the contour plot in Figure 5. This is because the curvature of the nanotube forces the highly responsive π system to the outside of the nanotube. There, extended currents circulate on a path that encompasses the entire nanotube, thus creating the strong magnetic response typical for aromatic CNTs.

Longitudinal Current Densities j_z^{ind}. Remarkably, the *longitudinal* currents j_z^{ind} of chiral nanotubes in an external magnetic field along the tube axis point to an interesting physical effect. Such currents parallel to the external field are usually weak because they are only *indirectly* induced. Specifically, in an isotropic medium, a magnetic field should give rise to currents which are always orthogonal to the field. Only when the spatial symmetry is broken, the currents will have a component parallel to the applied field. In molecules, this symmetry breaking naturally occurs *via* the chemical bonds (since in general they are not strictly parallel or orthogonal to the magnetic field). However, in molecules, the resulting parallel currents are highly localized. Upon integration with respect to the induced magnetic field, these currents give rise to non-vanishing off-diagonal elements of the nuclear shielding tensor, affecting only the region near the nuclei.

Further, we integrate the component of the current density j_z^{ind} within the (*x*, *y*)-plane *via* equation

$$j_{proj,z}^{ind}(x,y) = \frac{1}{L}\int_{z=0}^{L} dz\, j_z^{ind}(\mathbf{r}) \qquad (3)$$

where *L* is the size of the unit cell in our calculations. In Figure 7, we have plotted such current densities j_z^{ind} and $j_{proj,z}^{ind}$ for a (12,4) CNT with the external field along *Z*, *i.e.*, collinear with the tube. Both inside and outside the tube, there is a net current density of significant magnitude *parallel* to the magnetic field, while in a thin layer near the actual tube walls, this current vanishes. For comparison, in the non-chiral (11,0) tube, these integrated currents $j_{proj,z}^{ind}$ are much weaker and have alternating signs. Thus, only in chiral nanotubes there are significant net currents along the tube axis.

At first sight, these data seem to contradict the symmetry properties of magnetic fields, which are axial vectors. Normally, a magnetic field should not induce any net current density flux *parallel* to that field. However, this argument is valid only if the considered system itself is invariant under mirror symmetry. This is the case for non-chiral (*n*,0) tubes, but *not* for the chiral ones, which change their chirality upon application of a mirror symmetry. Consequently, we do not observe this parallel net current for non-chiral tubes. The interest-

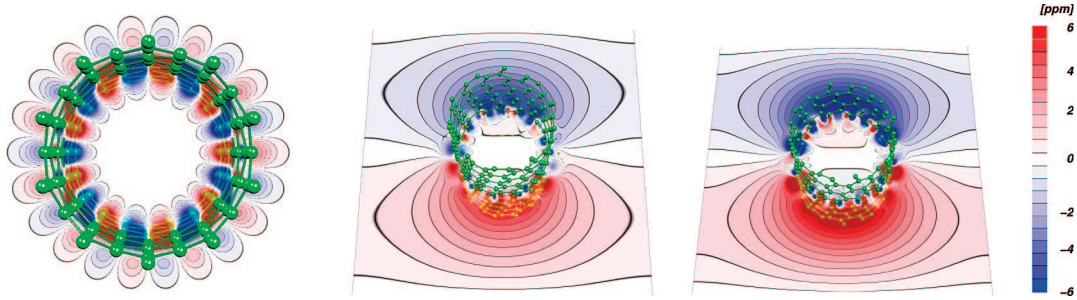

Figure 8. Horizontal components B_x^{ind} of the induced fields for non-chiral (left, (10,0) type) and chiral tubes (middle and right, (10,5) and (12,4) types). The externally applied field is oriented along the *Z* axis. For the (12,4) CNT, the response is so strong that the areas with weak intensity are already connected to their images in the tubes in the neighboring unit cells.

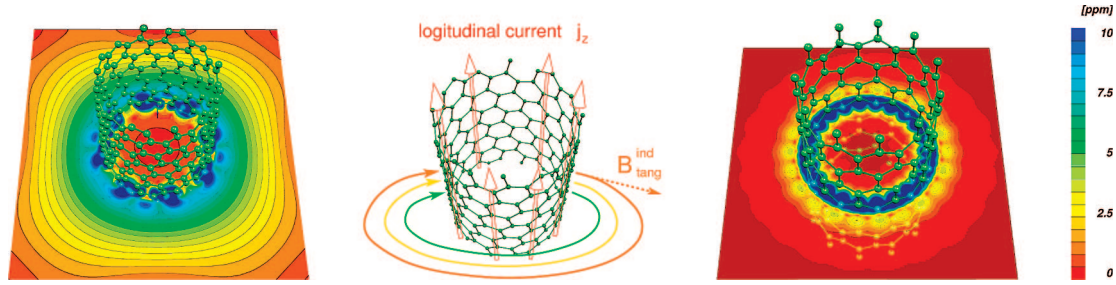

Figure 9. Left: Magnitudes of the tangential in-plane component of the induced magnetic field B^{ind}_{tang} for a (12,4) tube (left) and a (11,0) tube (right), for the externally applied field oriented along the *Z* axis. The schematic in the middle illustrates the field lines induced by an electronic current in a linear wire. The rectangular bias of the contour lines toward the borders is caused by the rectangular shape of our unit cell.

ing thing about our observation is that a chiral tube could act like a conventional coil made from wires, in which there is also a net transport of charge in the direction of the magnetic field.

Tangential Component of the Field Induced by j^{ind}_z. The longitudinal currents j^{ind}_z described above will translate into induced magnetic fields with components in *X* and *Y* directions, *i.e.*, in the plane orthogonal to the tube. In Figure 8, the *X*-components B^{ind}_x of the induced fields are plotted (still assuming an externally applied field oriented along the *Z* axis, parallel to the tube). Such a component B^{ind}_x can only be induced from a net current *along* the tube. However, as mentioned above, such a longitudinal current is not naturally created from the external field, since the latter is *parallel* to the CNT. Normally, such fields can only induce *perpendicular* ring currents; only in combination with a broken symmetry (here with respect to the inversion $Z \mapsto -Z$) is a significant net current parallel to the external field possible.

In a *non-chiral* CNT, the tangential induced field is mostly absent, as is demonstrated on the example of a (10,0) nanotube (left part of Figure 8). While close to the tube B^{ind}_x is weakly non-zero and oscillates, there is no long-range effect. The situation is entirely different for the chiral tubes (right part of Figure 8), where a strong positive *X*-component is visible above the tube, while the same field with opposite sign is observed below.

The components of the field induced by the j^{ind}_z current components can be analyzed further, similarly to the decomposition of the current densities, into longitudinal and tangential/radial components in analogy to eqs 1 and 2. In Figure 9, the tangential components $B^{ind}_{tang}(\mathbf{r}) = \hat{\mathbf{r}}_{tang} \cdot \mathbf{B}^{ind}(\mathbf{r})$ of the field are plotted for a chiral (12,4) and a non-chiral (11,0) nanotube. The schematic in the middle illustrates the field lines (solid lines) induced by an electronic current in a linear wire. The orientation of the tangential field vector $B^{ind}_{tang}(\mathbf{r})$ is also shown (dotted arrow). The magnitudes of $B^{ind}_{tang}(\mathbf{r})$ for two nanotubes are plotted in the left and right images of Figure 9.

In the chiral tube, we observe that this tangential field is rather large and decays with the distance to the tube. This is the behavior that is expected for the field created by a current in a linear wire (see the schematic in Figure 9). In contrast, there is essentially no tangential field component in the non-chiral CNT (right plot).

Thus we observe that, in the chiral CNTs, an effective (electronic) current in the direction of the externally applied field j^{ind}_z (*i.e.*, parallel to the tube axis) induces concentric magnetic field lines with non-vanishing tangential components B^{ind}_{xy}, as illustrated in the schematic in Figure 9. The overall effect of such a current is the conversion of the longitudinal magnetic field into the long-range tangential one.

CONCLUSION

In summary, by utilizing the state-of-the-art first-principles electronic structure approach, we have investigated the magnetic linear response of a series of achiral and chiral carbon nanotubes with diameters between 5 and 14 Å. We have found ^{13}C NMR chemical shifts to be in the range of 110−130 ppm, depending on the nanotube type, with larger tubes yielding lower shifts. These values are in reasonable agreement with the earlier work on the subject.[20]

As a consequence of these electronic response properties, a guest molecule experiences a screening of externally applied magnetic fields when located in a host superstructure. In double-wall carbon nanotubes, this effect is visible as a change in the NMR resonances of the inner tube, which has been proven experimentally by selective ^{13}C isotope substitution in the inner tube, leading to a distribution of the chemical shift tensor parameters.[24] Similar effects have been observed experimentally for smaller host molecules.[18]

The nucleus-independent induced shift inside the tubes is −60 to −30 ppm, with larger tubes yielding more negative values. For the coaxial (10,0)@(19,0) double wall nanotube system, we find that the NICS shift inside the innermost tube is the sum of the two single-wall nanotube values, thus manifesting the superposition principle. The ^{13}C shift change of the inner tube is in perfect agreement with the NICS map prediction. These NICS maps offer a convenient route to predict the shielding induced by nanotubes on the nearby molecules without any actual calculations.

Finally, we find that in chiral nanotubes, external *longitudinal* magnetic fields induce *longitudinal* current

densities, which in turn yield long-range *tangential* magnetic fields outside the tubes. The overall effect of such a current is the conversion of the longitudinal magnetic field into the long-range tangential one. Such a phenomenon is in sharp contrast to what is observed for non-chiral CNTs, where such currents are very short-ranged and there are no long-range tangential fields. While the isotropic NICS shift is virtually zero outside achiral tubes and small outside chiral tubes, the tangential component (for a parallel external magnetic field) is quite noticeable, with 5 ppm observed about 3 Å away from the (12,4) tube.

METHODS AND COMPUTATIONAL DETAILS

We have computed the electronic linear response to an external magnetic field **B** with Kohn–Sham density functional theory,[38] using the CPMD simulation package.[39] We have used the BLYP exchange-correlation functional[40,41] and a plane-wave basis set with a 50 Ry kinetic energy cutoff for the valence orbitals. Goedecker-type pseudopotentials[42] were used to describe the interaction of the valence shell with the nuclei and their core electrons. The geometric conformations and lattice parameters of the nanotubes were obtained from the TubeGen program.[43] The CC bond lengths in generated nanotubes were uniformly set to the graphitic value of 1.421 Å using TubeGen.

All calculations of NICS maps[25,44,45] have been carried out using the Density Functional Perturbation Theory module,[46,47] designed for calculations under periodic boundary conditions. NICS maps are a generalization of nuclear magnetic shielding tensors whose calculation is implemented within the same package.[48,49] For the NICS functions, we use the definition

$$\delta^{NICS}(\mathbf{r}) = -\frac{1}{3}\,\mathrm{Tr}\,\sigma(\mathbf{r}) \tag{4}$$

where Tr σ represents the trace of the nuclear shielding tensor. ^{13}C NMR chemical shifts are obtained indirectly by referencing the computed nuclear shieldings to those of benzene. This value is then further converted using the experimental TMS shift of $\delta_C^{TMS}(C_6H_6) = 131$ ppm [50,51] *via*

$$\delta_C^{calc}(X) = \delta_C^{exp}(C_6H_6) + \sigma_C(C_6H_6) - \sigma_C(X) \tag{5}$$

Here, $\sigma_C(X)$ denotes the nuclear shielding of a carbon atom in molecule X, and $\delta_C(X)$ refers to the corresponding NMR chemical shift. Both quantities are dimensionless, as the shielding is essentially the proportionality constant between external and induced magnetic field. Since σ is usually very small, it is commonly quoted in parts per million (ppm). All visualizations were done with the Molekel program[52] and post-processed with the GIMP package.[53]

All properties required for the calculation of our NICS maps are computed in reciprocal space (**G**-space), using fast Fourier transform techniques to switch to direct space and *vice versa*.[23] For all calculations, we have used large supercells, which enable us to restrict the *k*-point sampling to the Γ-point. We have performed an explicit calculations of the (10,0) tube using both four and eight repeat units. The energy difference was only 0.1 kcal/mol, while the ^{13}C NMR chemical shifts and the inner NICS fields decreased by about 5 and 9 ppm, respectively. This indeed represents a source of error in our calculations, but it only affects the results quantitatively (not in the overall features that we chose to focus on). Considering that the semiconducting nanotubes under study have similar band gaps, we aimed to keep the length of the nanotube unit cell roughly the same across all tubes studied, in order to ensure that the predicted trends within the nanotube series are meaningful. In a previous work,[21] a comparable convergence of the shieldings with the *k*-point mesh has been observed for larger-gap CNTs.

Another source of error in predicted magnetic response properties is the CNT geometry. We have done a geometry optimization of a (10,0) nanotube, finding that the energy gain upon optimization was about 0.3 kcal/mol (per carbon). Also, after the optimization, the NMR chemical shifts of the carbon atoms changed by only 1.5 ppm, while the NICS values were somewhat more affected ($\Delta\delta^{NICS} \approx 4$ ppm). We deemed such differences unimportant within the much larger trends found for nanotubes of different diameters, and for reasons of computational efficiency, we proceeded without structural optimizations, setting all CC bond lengths to 1.421 Å.

Finally, we should note that these are some of the largest NMR calculations to date, with 464 atoms in the unit cell for the (10,0)@(19,0) double-walled tube. The efficiently parallelized implementation of magnetic field response takes less than 24 h for the 464-atom system on 128 Pentium4 CPUs at 3.2 GHz. Another work has recently reported an NMR calculation for a larger non-periodic 1003-atom system, which, however, did not provide the absolute wall times.[54]

Acknowledgment. D.S. acknowledges support from the DFG under grant SFB 625. KNK acknowledges financial support from the National Science Foundation NIRT under Grant No. CMS-0609049.

REFERENCES AND NOTES

1. Iijima, S. Helical Microtubules of Graphitic Carbon. *Nature* **1991**, *354*, 56–58.
2. Saito, R.; Dresslhaus, G.; Dresselhaus, M. S. *Physical Properties of Carbon Nanotubes*; Imperial College Press: London, 1998.
3. Thess, A.; Lee, R.; Nikolaev, P.; Dai, H.; Petit, P.; Robert, J.; Xu, C.; Lee, Y. H.; Kim, S. G.; Colbert, D. T.; *et al.* Crystalline Ropes of Metallic Carbon Nanotubes. *Science* **1996**, *273*, 483.
4. Harris, P. J. F. *Carbon Nanotubes and Related Structures*; Cambridge University Press: Cambridge, UK, 1999.
5. Barone, V.; Peralta, J. E.; Wert, M.; Heyd, J.; Scuseria, G. E. Density Functional Theory Study of Optical Transitions in Semiconducting Single-Walled Carbon Nanotubes. *Nano Lett.* **2005**, *5*, 1621–1624.
6. Ivanovskaya, V. V.; Ranjan, N.; Heine, T.; Merino, G.; Seifert, G. Molecular Dynamics Study of the Mechanical and Electronic Properties of Carbon Nanotubes. *Small* **2005**, *1*, 399–402.
7. Kudin, K. N.; Scuseria, G.; Yakobson, B. I. C2F, BN, and C Nanoshell Elasticity from Ab-Initio Computations. *Phys. Rev. B* **2001**, *64*, 235406.
8. Wang, B.; Král, P. Chemically Tunable Nanoscale Propellers of Liquids. *Phys. Rev. Lett.* **2007**, *98*, 266102.
9. Kozinsky, B.; Marzari, N. Static Dielectric Properties of Carbon Nanotubes from First Principles. *Phys. Rev. Lett.* **2006**, *96*, 166801.
10. Brothers, E.; Scuseria, G.; Kudin, K. Longitudinal Polarizability of Carbon Nanotubes. *J. Phys. Chem. B* **2006**, *110*, 12860–12864.
11. Brothers, E.; Scuseria, G.; Kudin, K. Coaxial Carbon Nanotubes as Shielded Nanowires. *J. Chem. Phys.* **2006**, *124*, 041101.
12. Brothers, E.; Izmaylov, A. F.; Scuseria, G.; Kudin, K. Analytically Calculated Polarizability of Carbon Nanotubes: Single Wall, Coaxial, and Bundled Systems. *J. Phys. Chem. C* **2008**, *112*, 1396–1400.
13. Snow, E.; Perkins, F. Capacitance and Conductance of Single-Walled Carbon Nanotubes in the Presence of Chemical Vapors. *Nano Lett.* **2005**, *5*, 2414–2417.
14. Matsuo, Y.; Tahara, K.; Nakamura, E. Theoretical Studies on Structures and Aromaticity of Finite-Length Armchair Carbon Nanotubes. *Org. Lett.* **2003**, *5*, 3181–3184.

15. Lier, G. V.; Fowler, P. W.; Proft, F. D.; Geerlings, P. A Pentagon-Proximity Model for Local Aromaticity in Fullerenes and Nanotubes. *J. Phys. Chem. A* **2002**, *106*, 5128–5135.
16. Clewett, C. F. M.; Pietra, T. ^{129}Xe and ^{131}Xe NMR of Gas Adsorption on Single- and Multi-Walled Carbon Nanotubes. *J. Phys. Chem. B* **2005**, *109*, 17907–17912.
17. Mao, S.; Kleinhammes, A.; Wu, Y. NMR Study of Water Adsorption in Single-Walled Carbon Nanotubes. *Chem. Phys. Lett.* **2006**, *421*, 513–517.
18. Sekhaneh, W.; Kotecha, M.; Dettlaff-Weglikowska, U.; Veeman, W. S. High Resolution NMR of Water Absorbed in Single-Wall Carbon Nanotubes. *Chem. Phys. Lett.* **2006**, *428*, 143–147.
19. Liu, Z.; Sun, X.; Nakayama-Ratchford, N.; Dai, H. Supramolecular Chemistry on Water-Soluble Carbon Nanotubes for Drug Loading and Delivery. *ACS Nano* **2007**, *1*, 50–56.
20. Marques, M. A. L.; d'Avezac, M.; Mauri, F. Magnetic Response and NMR Spectra of Carbon Nanotubes from Ab-Initio Calculations. *Phys. Rev. B* **2006**, *73*, 125433.
21. Zurek, E.; Pickard, C. J.; Walczak, B.; Autschbach, J. Density Functional Study of the ^{13}C NMR Chemical Shifts in Small-to-Medium-Diameter Infinite Single-Walled Carbon Nanotubes. *J. Phys. Chem. A* **2006**, *110*, 11995–12004.
22. Besley, N. A.; Titman, J. J.; Wright, M. D. Theoretical Study of the ^{13}C NMR Spectroscopy of Single-Walled Carbon Nanotubes. *J. Am. Chem. Soc.* **2005**, *127*, 17948–17953.
23. Sebastiani, D. Current Density Plots and Nucleus Independent Chemical Shift Maps (NICS) from Reciprocal Space Density Functional Perturbation Theory Calculations. *ChemPhysChem* **2006**, *7*, 164–175.
24. Simon, F.; Kramberger, C.; Pfeiffer, R.; Kuzmany, H.; Zólyomi, V.; Kürti, J.; Singer, P. M.; Alloul, H. Isotope Engineering of Carbon Nanotube Systems. *Phys. Rev. Lett.* **2005**, *95*, 017401.
25. Schleyer, P. v. R; Maerker, C; Dransfeld, A; Jiao, H.; Hommes, N. J. R. v. E. Nucleus-Independent Chemical Shifts: A Simple and Effcient Aromaticity Probe. *J. Am. Chem. Soc.* **1996**, *118*, 6317–6318.
26. Ndungu, S, S. B.; P.; Bradley, J. C.; Rossi, M. P.; Gogotsi, Y. Guiding Water Into Carbon Nanopipes With the Aid of Bipolar Electrochemistry. *Microfluidics Nanofluidics* **2005**, *1*, 284–288.
27. Reiter, G. F.; Burnham, C.; Homouz, D.; Platzman, P. M.; Mayers, J.; Abdul-Redah, T.; Moravsky, A. P.; Li, J. C.; Loong, C. K.; Kolesnikov, A. I. Anomalous Behavior of Proton Zero Point Motion in Water Confined in Carbon Nanotubes. *Phys. Rev. Lett.* **2006**, *97*, 247801.
28. Pietra, T.; Shen, K. NMR Spectroscopy of Hydrogen Adsorption on Single-Walled Carbon Nanotubes After Exposure to High Pressure. *Solid State Nucl. Magn. Reson.* **2006**, *29*, 125–131.
29. Mpourmpakis, G.; Froudakis, G. E.; Lithoxoos, G. P.; Samios, J. Effect of Curvature and Chirality for Hydrogen Storage in Single-Walled Carbon Nanotubes: A Combined Ab Initio and Monte Carlo Investigation. *J. Chem. Phys.* **2007**, *126*, 144704.
30. Zhou, W.; Han, Z.; Wang, J.; Zhang, Y.; Jin, Z.; Sun, X.; Zhang, Y.; Yan, C.; Li, Y. Copper Catalyzing Growth of Single-Walled Carbon Nanotubes on Substrates. *Nano Lett.* **2006**, *6*, 2987–2990.
31. Takagi, D.; Homma, Y.; Hibino, H.; Suzuki, S.; Kobayashi, Y. Single-Walled Carbon Nanotube Growth from Highly Activated Metal Nanoparticles. *Nano Lett.* **2006**, *6*, 2642–2645.
32. Chorro, M.; Delhey, A.; Noé, L.; Monthioux, M.; Launois, P. Orientation of C_{70} Molecules in Peapods as a Function of the Nanotube Diameter. *Phys. Rev. B* **2007**, *75*, 035416.
33. Hoffmann, A.; Sebastiani, D.; Sugiono, E.; Kim, K. S.; Spiess, H. W.; Schnell, I. Solvent Molecules Trapped in Supramolecular Organic Nanotubes: A Combined Solid-State NMR and DFT Study. *Chem. Phys. Lett.* **2004**, *388*, 164–169.
34. Douglas, T.; Young, M. Host-Guest Encapsulation of Materials by Assembled Virus Protein Cages. *Nature* **1998**, *393*, 152–155.
35. Cheetham, A. K.; Ferey, G.; Loiseau, T. Open-Framework Inorganic Materials. *Angew. Chem., Int. Ed.* **1999**, *38*, 3268–3292.
36. Holliday, B. J.; Mirkin, C. Strategies for the Construction of Supramolecular Compounds through Coordination Chemistry. *Angew. Chem., Int. Ed.* **2001**, *40*, 2022–2043.
37. Koshino, M.; Tanaka, T.; Solin, N.; Suenaga, K.; Isobe, H.; Nakamura, E. Imaging of Single Organic Molecules in Motion. *Science* **2007**, *316*, 853.
38. Jones, R. O.; Gunnarsson, O. The Density Functional Formalism, Its Applications and Prospects. *Rev. Mod. Phys.* **1989**, *61*, 689–746.
39. Hutter, J.; Curioni, A. Car-Parrinello Molecular Dynamics on Massively Parallel Computers. *ChemPhysChem* **2005**, *6*, 1788–1793.
40. Becke, A. D. Density-Functional Exchange-Energy Approximation With Correct Asymptotic Behavior. *Phys. Rev. A* **1988**, *38*, 3098.
41. Lee, C.; Yang, W.; Parr, R. G. Development of the Colle-Salvetti Correlation-Energy Formula into a Functional of the Electron-Density. *Phys. Rev. B* **1988**, *37*, 785–789.
42. Hartwigsen, C.; Goedecker, S.; Hutter, J. Relativistic Separable Dual-Space Gaussian Pseudopotentials from H to Rn. *Phys. Rev. B* **1998**, *58*, 3641.
43. Frey, J. T.; Doren, D. J. *TubeGen software*, version 3.3; 2005 (turin.nss.udel.edu/research/tubegenonline.html).
44. Heine, T.; Schleyer, P. v. R; Corminboeuf, C; Seifert, G; Reviakine, R; Weber, J. Analysis of Aromatic Delocalization: Individual Molecular Orbital Contributions to Nucleus-Independent Chemical Shifts. *J. Phys. Chem. A* **2003**, *107*, 6470–6475.
45. Kirchner, B.; Sebastiani, D. Visualizing Degrees of Aromaticity. *J. Phys. Chem. A* **2004**, *108*, 11728–11732.
46. Baroni, S.; de Gironcoli, S.; del Corso, A.; Giannozzi, P. Phonons and Related Crystal Properties from Density-Functional Perturbation Theory. *Rev. Mod. Phys.* **2001**, *73*, 515.
47. Putrino, A.; Sebastiani, D.; Parrinello, M. Generalized Variational Density Functional Perturbation Theory. *J. Chem. Phys.* **2000**, *113*, 7102–7109.
48. Sebastiani, D.; Parrinello, M. A New Method to Compute NMR Chemical Shifts in Periodic Systems. *J. Phys. Chem. A* **2001**, *105*, 1951.
49. Sebastiani, D.; Goward, G.; Schnell, I.; Spiess, H. W. NMR Chemical Shifts in Proton Conducting Crystals from First Principles. *J. Mol. Struct. (THEOCHEM)* **2003**, *625*, 283–288.
50. Jameson, A.; Jameson, C. Gas-Phase C-13 Chemical-Shifts in the Zero-Pressure Limit—Refinements to the Absolute Shielding Scale for C-13. *Chem. Phys. Lett.* **1987**, *134*, 461.
51. Gottlieb, H. E.; Kotlyar, V.; Nudelman, A. NMR Chemical Shifts of Common Laboratory Solvents as Trace Impurities. *J. Org. Chem.* **1997**, *62*, 7512–7515.
52. Flükiger, P.; Lüthi, H. P.; Portmann, S.; Weber, J. *Molecular Visualization Program Molekel*, Version 4.0; Swiss Center for Scientific Computing: Manno, Switzerland; 2000.
53. Kimball, S.; Mattis, P *GNU Image Manipulation Program GIMP*, version 2.0; released under the GNU public license (http://www.gimp.org).
54. Ochsenfeld, C.; Kussmann, J.; Koziol, F. Ab Initio NMR Spectra for Molecular Systems with a Thousand and More Atoms: A Linear-Scaling Method. *Angew. Chem., Int. Ed.* **2004**, *43*, 4485–4489.